Time evolution of Kirkendall porosity in single-phase Ni-based diffusion couples

Camille Salsi, Julien Lesseur, Daniel Monceau, Clara Desgranges, Thomas Gheno

Acta Materialia 293 (2025) 121022

Contents lists available at ScienceDirect

Acta Materialia

journal homepage: www.elsevier.com/locate/actamat

Full length article

Time evolution of Kirkendall porosity in single-phase Ni-based diffusion couples

Camille Salsi [a], Julien Lesseur [b], Daniel Monceau [c], Clara Desgranges [d], Thomas Gheno [a,*]

[a] DMAS, ONERA, Université Paris-Saclay, 92320, Châtillon, France
[b] IRT Saint Exupéry, 3 rue Tarfaya, 31405 Toulouse, France
[c] CIRIMAT, Université de Toulouse, CNRS, INP-ENSIACET, 4 allée Emile Monso, 31030 Toulouse, France
[d] Université Paris-Saclay, CEA, SC2M, 91191, Gif-sur-Yvette, France

ARTICLE INFO

Keywords:
Interdiffusion
Vacancies
Grain boundaries
Microstructure
Microtomography

ABSTRACT

The development of the Kirkendall porosity was studied in fcc Ni–30Cr/Ni–10Si diffusion couples at 1176 °C using X-ray tomography, optical and scanning electron microscopy, and multicomponent diffusion simulation. Diffusion experiments were interrupted multiple times to monitor the porosity ex situ by tomography. This allowed tracking the position and size of thousands of pores over tens of hours. Pores detected by tomography were also observed by microscopy to determine the surrounding grain structure. The porosity depth profiles (number density, equivalent diameter, area/volume fraction) derived from 2D cross-sectional observations and 3D tomography were compared and the benefits of both methods discussed. Alloys of different grain sizes were used as starting materials to study the influence of the grain boundary density on the spatial pore distribution. Local analysis showed that pore nucleation was not significantly accelerated on grain boundaries compared to the grain interior, but that pore growth was faster along grain boundaries. The time-resolved pore distribution data indicated that the porosity evolved through both pore movement and growth-shrinkage. These mechanisms were discussed in view of the simulated vacancy flux profile.

1. Introduction

The properties of high temperature materials rely on optimized compositions and microstructures. These may evolve over time as diffusion proceeds, driven by chemical potential gradients present from manufacturing or generated in service. In an alloy-coating system, for example, where the alloy is designed for mechanical resistance and the coating provides protection against corrosion, interdiffusion tends to degrade the properties of both components, causing the precipitation of undesired phases in the alloy and reducing the availability of the protective element in the coating [1–4].

In addition to composition and phase changes, interdiffusion may induce porosity, plastic deformation or stress due to the Kirkendall effect [5–7]. In a multicomponent material subject to diffusion, differences in atom mobilities result in unbalanced atom fluxes, compensated by a vacancy flux. The latter tends to locally steer the vacancy concentration away from its equilibrium value, which in turn triggers vacancy creation and annihilation by crystalline defects, acting as sources and sinks [8]. Vacancy creation/annihilation by dislocation climb produces a local translation of the crystal lattice called Kirkendall shift. The latter may generate plastic deformation and stress, depending on the materials properties and geometry [9–13]. Excess vacancies may also condense into pores [14,15], whose surfaces act as supplementary sinks. Kirkendall pores may locally occupy a significant fraction of the material and threaten its integrity [16,17].

The Kirkendall effect has been widely studied, both experimentally [18–26] and numerically [27–38]. However, despite being both of fundamental interest and of practical importance, the role of the microstructure (grain size and shape, dislocation density and organization) is poorly documented. Grain boundaries, heterophase interfaces and free surfaces are known as efficient point defect sinks, i.e., they are more potent sinks than the grain interior is. In the context of nuclear energy systems, it has been shown that increasing the density of interfaces led to enhanced defect trapping and therefore improved irradiation resistance (see Ref. [39] and citations therein). In the same way, lowering the grain size of a polycrystalline material could reduce the vacancy supersaturation generated by the Kirkendall effect, and therefore mitigate the development of Kirkendall porosity. As far as we know, this hypothesis has not been tested experimentally so far. Simulations of interdiffusion have been produced where the sink strength is

* Corresponding author.
E-mail address: thomas.gheno@onera.fr (T. Gheno).

https://doi.org/10.1016/j.actamat.2025.121022
Received 31 January 2025; Accepted 5 April 2025
Available online 23 April 2025

null in the grain interiors and infinite at grain boundaries [8]. This hypothesis is interesting theoretically but overestimates the sink strength contrast observed in practice. Simulations of this kind describing the behavior of real polycrystalline alloys have not been produced so far by lack of sink strength data.

Experimentally, the Kirkendall porosity produced by interdiffusion is most often studied by observing cross-sections of diffusion couples in a microscope. Cross-sectional examination covers a limited sample of the pore population. Further, it is destructive, and therefore cannot be used to monitor the time evolution of the porosity in a given specimen. Audigié et al. [26,35] and Epishin et al. [25] recently studied the Kirkendall porosity in Ni-based diffusion couples by synchrotron X-ray tomography, with sub-micron resolution. The use of tomography allowed the latter to study the pore shapes in relation with their location along the diffusion direction.

The aim of the present paper is to better understand the mechanisms underlying the development of the Kirkendall porosity, in particular with respect to the alloy grain structure. Grain boundaries tend to act as effective vacancy sinks, possibly mitigating pore development as mentioned above, but may also favor pore nucleation and growth. We seek to examine how these two apparently antagonist effects manifest both locally around a grain boundary and globally at the scale of the polycrystal. We also seek to determine the mechanisms by which a population of Kirkendall pores extends into an alloy as diffusion proceeds.

To do so, we used a combination of diffusion experiments and simulations in a couple made from alloys in the fcc phase of the Ni–Cr–Si system. The Ni–Cr system was chosen because it constitutes the base of many high temperature alloys. The diffusivities of nickel and chromium are quite similar, which yields a weak Kirkendall effect. Silicon was added because it produces large diffusivity differences in the system, which in turns gives rise to a stronger Kirkendall effect [40,41]. Furthermore, the Ni–Cr–Si system possesses a relatively large fcc domain at high temperature, which allows building single-phase couples with large composition gradients. Diffusion experiments were performed on alloys with different grain sizes. The Kirkendall porosity was studied from micrographs recorded by optical and scanning electron microscopy on cross-sections, and from 3D reconstructions obtained by X-ray tomography with a laboratory instrument. One couple was subjected to an interrupted diffusion test, and the same zone was analyzed by tomography at each interruption to monitor the porosity over time. We show how these techniques can be combined to examine the relationships between pore development and grain structure at the local scale (individual pores) and at the global scale (pore population). Diffusion simulations in 1D were used to evaluate the divergence of the vacancy flux, which drives pore development. These results are used to discuss the time evolution of the porosity observed experimentally.

2. Materials and methods

2.1. Experimental

2.1.1. Materials and diffusion tests

Alloys with nominal composition (at. %) Ni–30Cr and Ni–10Si were produced by vacuum induction melting and homogenized 24 h at 1250 °C in vacuum (10^{-4} mbar). The homogenized materials were single-phase fcc and had mm-size grains. Concentrations measured by scanning electron microscopy - energy dispersive spectrometry (SEM-EDS) were 29.1 at. % Cr and 10.4 at. % Si, respectively. Part of the Ni–30Cr ingot was cold-rolled to an 80% thickness reduction. The cold-rolled material was divided in three parts that were then subjected to different recrystallization heat treatments. These were designed to obtain three grain size categories: fine (~30 μm), medium (~300 μm) and coarse (>1 mm). The grain sizes were measured by the intercept method on cross-sections etched with Marble's reagent (HCl + $CuSO_4$ + H_2O). The time and temperature of these heat treatments are given in Table 1.

Table 1
Parameters of the recrystallization heat treatments applied to the cold-rolled Ni–30Cr alloy to obtain different grain sizes.

Condition	Time (h)	Temperature (°C)	Grain size (μm)
As-homogenized			>1000
Cold-rolled, recrystallized			
Fine-grained	1	885	30
Medium-grained	10	1176	300
Coarse-grained	48	1275	>1000

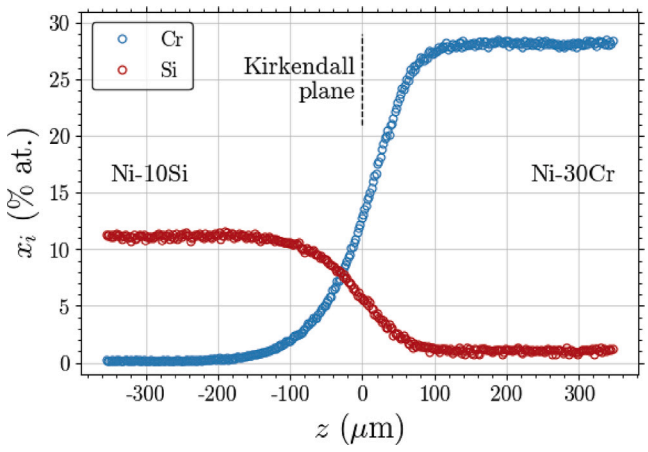

Fig. 1. Composition profile measured by SEM-EDS in Ni–30Cr/Ni–10Si couple after 10 h at 1176 °C. Couple prepared from an as-homogenized Ni–30Cr alloy (see Table 1).

The homogenized and recrystallized materials were cut into 6 × 6 × 1.5 mm samples by electric discharge machining. Diffusion couples Ni–30Cr / Ni–10Si were prepared according to the procedure described in Ref. [42]. Briefly, one face of each alloy was polished with SiC paper down to a P4000 grade. Particles of $Gd_2Zr_2O_7$ of average diameter 1 μm were deposited on one alloy to mark the location of the Kirkendall plane. The alloys were then placed between two plates of Ni-based superalloy Udimet 720 held together with molybdenum screws and nuts, and the assembly was heat-treated 1 h at 1050 °C in vacuum (10^{-4} mbar). The conditions were chosen so that the diffusion distance due to the assembly treatment (~10 μm) would be small compared to that of the diffusion tests (~100–400 μm). After the assembly treatment, the couples were cooled down and removed from the assembly device. The diffusion tests were conducted at 1176 °C in vacuum (10^{-4} mbar).

The grain size of the fine-grained recrystallized samples increased during the diffusion heat treatment, from 30 μm to about 200 μm in 10 h at 1176 °C. Grain growth slowed down over time, and an average grain size of about 200–300 μm was observed between 10 h and 70 h at 1176 °C. More details about the grain size evolution are given in Ref. [40].

2.1.2. Cross-section analyses

Diffusion experiments of duration 2, 10, 19, 24 and 100 h were performed on separate samples for cross-section analysis. Metallographic cross-sections were prepared by conventional methods. Concentration profiles were measured by SEM-EDS in a Zeiss Merlin field emission gun microscope operated at 10 kV, using pure metals as standards and the $\phi(\rho z)$ quantification method. The step size was 2 μm. An example of concentration profiles measured after 10 h diffusion is shown in Fig. 1: the interdiffusion zone is seen to extend over about 300 μm.

The Kirkendall porosity was studied from optical micrographs recorded using a Zeiss microscope, with a spatial resolution of about 0.2

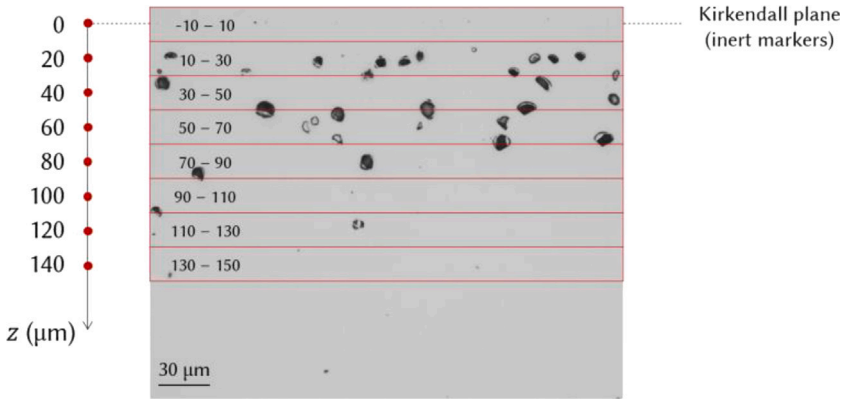

Fig. 2. Binning procedure used to generate porosity profiles from optical micrographs.

μm/pixel. The micrographs were binarized and analyzed using Fiji [43] to provide the position and surface area of each pore. Multiple images were combined to scan the 6 mm length of the cross-sections, which yielded about 500 to 1000 pores per sample. The spatial distribution of the pores (areal number density, equivalent diameter, surface fraction) was studied as a function of the distance to the Kirkendall plane by grouping pores in distance bins, as shown in Fig. 2. Individual pore surfaces were divided by the bin surfaces and combined to provide each point of the profile. Equivalent diameters were computed from the pore surface areas, assuming a circular shape.

2.1.3. X-ray tomography

Additional diffusion couples were prepared for analysis by X-ray tomography. Prior to the diffusion tests, the couples were cut from a 6 × 6 mm to a 2 × 2 mm basis (normal to the diffusion direction) to reduce the analyzed volume and thereby improve the spatial resolution. The analysis was performed using an EasyTom 230 microtomograph from RX Solutions, with a 100 kV tension and a 23 μA current. 1440 radiographic projections were continuously recorded through 360° rotation with a 3.3 s exposure time. 3D reconstruction was carried out with X-Act software (RX Solutions) using Feldkamp back projection algorithm [44]. The final reconstructed voxel size was 1.9 μm. Processing and visualization were done with Avizo for Industrial Inspections 2021.1 (ThermoFisher Scientific). A non-local mean filter and unsharp masking filter were applied prior to segmenting the data. The pores were segmented using an automatic entropy-based thresholding procedure. Individual pores with a diameter larger than 5 μm could be identified. The analyzed volume was 2 × 2 × 2 mm^3, which yielded about 7000 to 20 000 pores per couple. Fig. 3 shows an example of pore reconstruction obtained after a 24 h diffusion test. Pore distribution profiles (volumetric number density, equivalent diameter, volume fraction) were obtained by sorting the pores into bins based on their position from the Kirkendall plane. Equivalent diameters were computed from the pore volumes, assuming a spherical shape.

One couple was subjected to an interrupted diffusion test and analyzed by tomography at each interruption (2 h, 10 h, 19 h, 30 h and 70 h) to track pores over time. This required aligning the position of the datasets with respect to a common reference. One of the two alloys of the couple included large pores inherited from casting, away from the interdiffusion zone. The location, size (hundreds of μm) and shape of these pores ensured that they could not be mistaken with the Kirkendall pores. Their tortuous shape helped align the datasets and ensure that the displacements measured between two interruptions were due to diffusion. The movement of the Kirkendall pores between time stages was tracked based on their center coordinates. Pores from two successive stages were matched as follows: for each pore detected at a given time, we computed the Euclidean distance to all pores detected at the next interruption time; we then considered that the pair minimizing this distance represented the same pore, which had moved in the time interval. For each match, the displacements along the 3 axes were computed.

2.1.4. Comparison between porosity measurements by microscopy and tomography

The properties of the two analysis techniques were compared on the same sample, after a 10 h diffusion test; the results are summarized in Fig. 4. Given a large number of spherical pores with diameters drawn from a lognormal distribution, it can be shown that on average, the mean diameter of the disks measured on the cross-section is close to the mean pore diameter, and the surface fraction is close to the volume fraction (see Appendix A). Consequently, mean diameters measured by microscopy and tomography can be compared directly, as well as surface and volume fractions. However, the ratio between areal and volumetric number densities depends on the mean diameter; these quantities are plotted on separate axes in Fig. 4a.

The mean equivalent diameters obtained by the two techniques are markedly different (Fig. 4b), for the following reasons. Optical microscopy offers a sufficient resolution (0.2 μm/pixel) to measure micron-size pores accurately, but detects a large number of submicronic objects, part of which are artifacts due to surface preparation. This tends to drive down the mean diameter. Because of its lesser resolution (1.9 μm/voxel), tomography detects only pores with diameters larger than about 5 μm, and overestimates the size of the detected pores. Yet the surface and volume fraction profiles measured by microscopy and tomography, respectively, are very close (Fig. 4c). This apparent agreement is due to the fact that the measurement biases associated with each technique tend to compensate each other; it is fortuitous and should not hide the fact that both techniques have biases.

We conclude that optical microscopy offers a good sensitivity over a small sample size, while X-ray tomography with our laboratory instrument is much less sensitive but offers a much larger sample size. The limitations of the two techniques are different in nature but give rise to comparable estimations of the pore fraction profile. The two techniques are complementary; tomography has the advantage of being non-destructive.

2.2. Simulations

Diffusion was simulated in 1D by finite differences. The pore fraction was evaluated using a method adapted from Höglund and Ågren [45]. Briefly, a simulation is run assuming that dislocation climb (or any other lattice site creation/annihilation process) fully accommodates the vacancy supersaturation/undersaturation induced by the Kirkendall effect. Thus, vacancies are maintained at equilibrium, no porosity can develop, and the Kirkendall effect is entirely manifested in lattice shift. We refer to this as the "ideal lattice" hypothesis. A virtual pore fraction is then calculated as a post-processing step. The balance equation for vacancies is written:

$$\frac{1}{V_m}\frac{\partial y_{\mathrm{Va}}}{\partial t} = -\frac{\partial J_{\mathrm{Va}}}{\partial z} + \dot{q}\ , \tag{1}$$

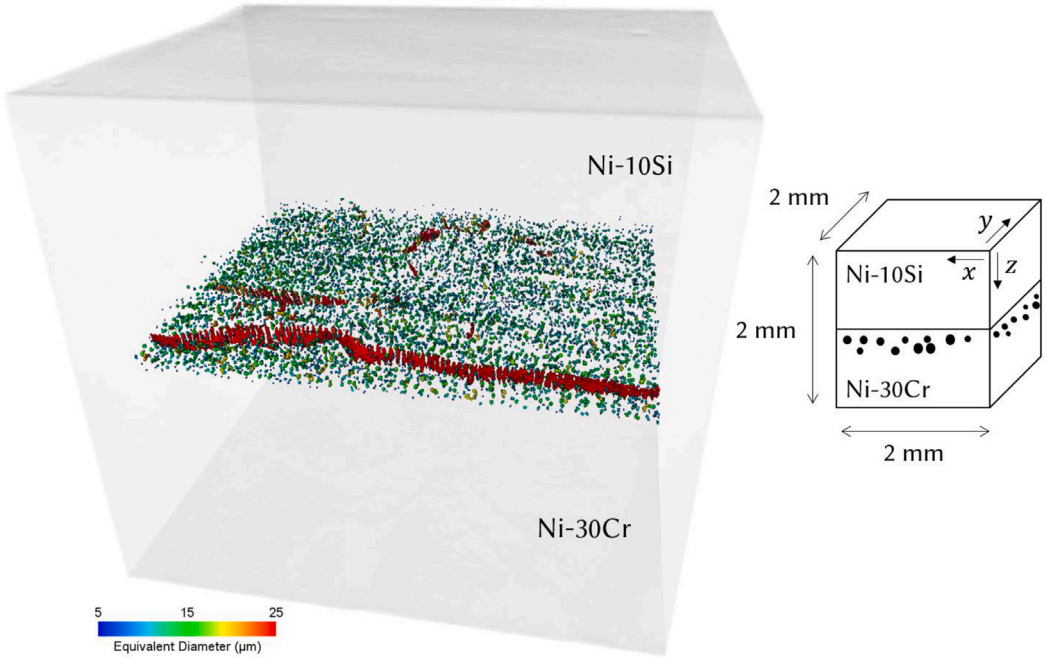

Fig. 3. Reconstruction of the porosity obtained by tomography in a Ni–30Cr/Ni–10Si couple after 24 h at 1176 °C. Couple prepared from an as-homogenized Ni–30Cr alloy. The pores are colored according to their size. (For interpretation of the references to color in this figure legend, the reader is referred to the web version of this article.)

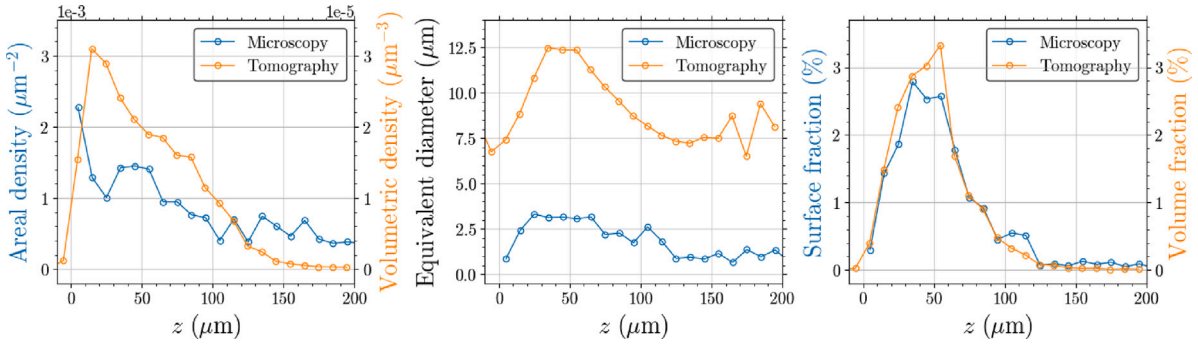

Fig. 4. Porosity distribution (density, equivalent diameter, fraction) measured in a Ni–30Cr/Ni–10Si couple annealed 10 h at 1176 °C, from optical micrographs and X-ray tomography. Data collected from a 6 mm long cross-section (microscopy) and a 2 × 2 × 2 mm^3 volume (tomography) were grouped in 10 μm bins, along the diffusion direction (see Fig. 2). The results are plotted against the distance to the Kirkendall plane, on the Ni–30Cr side.

where V_m is the alloy molar volume, which we assume is composition-independent, y_{Va} is the vacancy site fraction, $\boldsymbol{J}_{\mathrm{Va}}$ is the vacancy flux density (in mol m^{-2} s^{-1}) in the lattice-fixed reference frame, and $\dot{q}$ is a sink term representing the rate at which lattice sites are created/annihilated. The vacancy flux is obtained from the fluxes of the atomic species computed in the simulation:

$$\boldsymbol{J}_{\mathrm{Va}} = -\sum_{i=1}^{n} \boldsymbol{J}_i \,. \tag{2}$$

The ideal lattice hypothesis implies $\frac{\partial y_{\mathrm{Va}}}{\partial t} = 0$. Eq. (1) then yields:

$$\dot{q} = \frac{\partial J_{\mathrm{Va}}}{\partial z} \,. \tag{3}$$

The pore fraction f_p is then calculated as the quantity that would be obtained if, instead of being annihilated by dislocation climb, all excess vacancies had condensed into pores. It represents an upper bound of the true pore fraction. Assuming that the volume of a pore formed by one mole of vacancies is the alloy molar volume, f_p is obtained as:

$$f_p = -V_m \int_0^t \dot{q}\, \mathrm{d}t. \tag{4}$$

Finally, f_p is clipped to retain only positive values — this assumes that the vacancy deficit is accommodated by dislocation climb in undersaturation zones. This estimation of f_p relies on strong approximations. More elaborate estimation methods have been devised recently [36–38], which have their own advantages and disadvantages but all yield qualitatively similar results. As shown below, the input data used to run the simulation has a very important impact on the computed porosity. It follows that the upper bound provided by Eq. (4) is sufficient for the present purposes.

Simulations were run using three combinations of software and of thermodynamic and mobility databases (Table 2). Unsatisfactory agreement between the composition profiles obtained with existing mobility databases led us to determine our own mobility parameters, using the assessment by Du and Schuster [46] as a starting point: the optimization procedure is summarized in Appendix B. The composition profiles obtained with the three combinations are compared with the experimental data in Fig. 5. The simulated profiles are reasonably close to each other and to the experimental profiles: the agreement is slightly better with Du and Schuster database than with the TCS databases, and better still with our database — this was expected insofar as our database was optimized using a single data set, which includes the profile shown in Fig. 5: see Appendix B.

Table 2
Software and input data used in the diffusion simulations. TCS refers to Thermo-Calc Software.

Software	Thermodynamic database	Mobility database
Thermo-Calc [47]	TCNI8 (TCS)	MOBNI5 (TCS)
Noda [37]	Schuster and Du [48]	Du and Schuster [46]
Noda [37]	Schuster and Du [48]	Salsi [40]

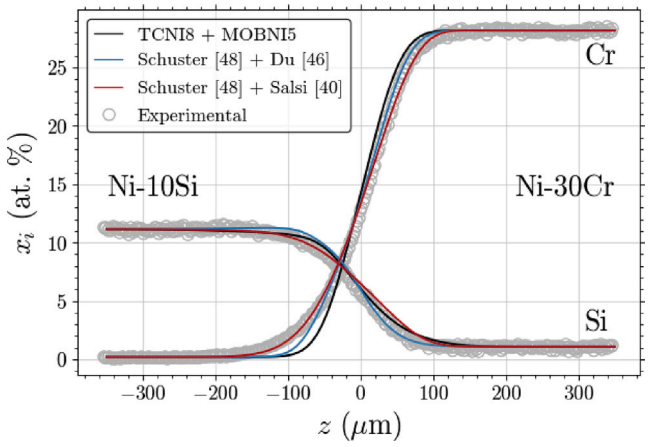

Fig. 5. Composition profiles in Ni–30Cr/Ni–10Si couple after 10 h at 1176 °C simulated with three database combinations (Table 2), and compared with the experimental data.

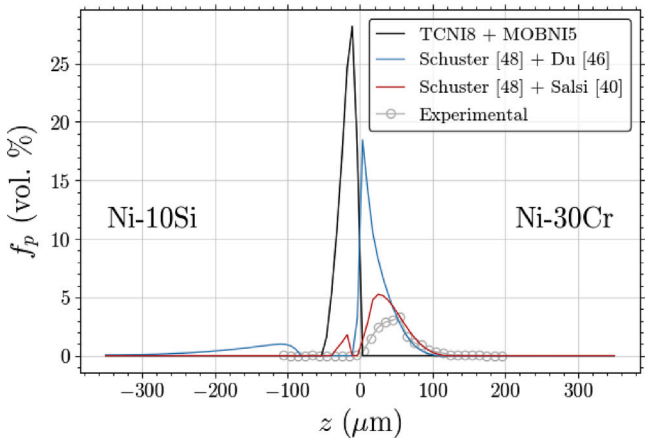

Fig. 6. Pore fraction profiles in Ni–30Cr/Ni–10Si couple after 10 h at 1176 °C computed using Eq. (4) and simulation results obtained with three database combinations (Table 2), compared with experimental data (tomography).

In contrast, the pore fraction profiles are strongly affected by the input data: with the TCS databases, pores are predicted to form on the Ni–10Si side and not on the Ni–30Cr side, while the reverse is predicted with the two other combinations, and observed experimentally (Fig. 6). The profile obtained with our mobility data is in reasonable agreement with the experimental profile, while that obtained with data from Du and Schuster features a peak that has a much sharper shape, is closer to the Kirkendall plane, and has a higher amplitude, compared to the experimental profile. We conclude that the simulation run with our mobility database is the most adequate to study porosity in the Ni–30Cr/Ni–10Si couple, and only this database is used in the following.

Simulation and data processing were done using Python scripts, relying on the Numpy [49], Scipy [50] and Matplotlib [51] libraries.

3. Results and discussion

The results are organized in two parts. First, we examine the role of grain boundaries on the Kirkendall porosity, by observing the morphology of the pore and grain structures, and by comparing pore distributions measured from samples with different grain sizes. In a second part, we study the mechanisms of porosity development, using time-resolved pore distribution data. These results are interpreted with the help of simulated vacancy flux profiles.

3.1. Role of grain boundaries

3.1.1. Local analysis

Couples diffusion-treated 2, 10, 19, 24 and 100 h were examined by optical microscopy and SEM. Kirkendall pores were distributed in a heterogeneous manner along the interdiffusion zone, and even within grains. The pores were not found to be more numerous on grain boundaries, nor depleted around grain boundaries. However, alignments of pores elongated along the diffusion direction were detected by tomography, as shown in Fig. 3. We identified such an alignment in a couple after a 19 h diffusion test, selected a slice containing an elongated pore, prepared a cross-section in the plane of this slice, and observed it by SEM. The images obtained by tomography and microscopy are compared in Fig. 7. The crystalline contrast on the SEM image highlights the grain structure and indicates that the elongated pore is located along a grain boundary.

The couples shown in Figs. 3 and 7 were prepared with an as-homogenized Ni–30Cr alloy, which had mm-size grains. A couple prepared using a fine-grained Ni–30Cr alloy (Table 1) was also analyzed by tomography. A top view reconstruction is shown in Fig. 8. After 10 h, the pore size and density are uniform. As time increases, a network of larger pores appears. This network is compatible, in its size and shape, with the grain structure. We conclude that pores located along the grain boundaries grow faster than those located within the grains. This is in general not visible from cross-sections presumably because cross-sections provide a small sample size and pores are not necessarily elongated in the cut plane.

3.1.2. Global analysis

The effect of the grain size on the total amount of pores was studied by comparing three couples prepared with Ni–30Cr alloys that had different initial grain sizes (Table 1). Pore distribution data obtained from optical micrographs, shown in Fig. 9, indicate that the initial grain size does not significantly affect the pore density, diameter or surface fraction. The absence of a visible grain size effect may have several causes, for instance:

- Pore growth is faster along some grain boundaries, but slower along others.
- Pore growth is on average faster along grain boundaries, but this is compensated by slower pore growth in the grains (i.e., the total volume of pores is unchanged).
- Pore growth is faster along grain boundaries than in the grains, but the difference is not large enough to produce a visible effect, in the grain size range investigated here.

An additional observation suggests that not all grain boundaries are equivalent with respect to the Kirkendall effect: the pore distribution is not the same whether the Ni–30Cr alloy has only been homogenized, or cold-rolled and recrystallized, with mm-large grains in both cases. As shown in Fig. 10, when the Ni–30Cr alloy is recrystallized, the pore density is larger, the mean diameter smaller, and the surface fraction slightly larger. Grain boundaries are curved and irregular in the as-homogenized microstructure, and straight in the recrystallized microstructure. This morphological difference is likely associated with structural differences, and, in turn, differences in the grain boundaries capacity to annihilate vacancies.

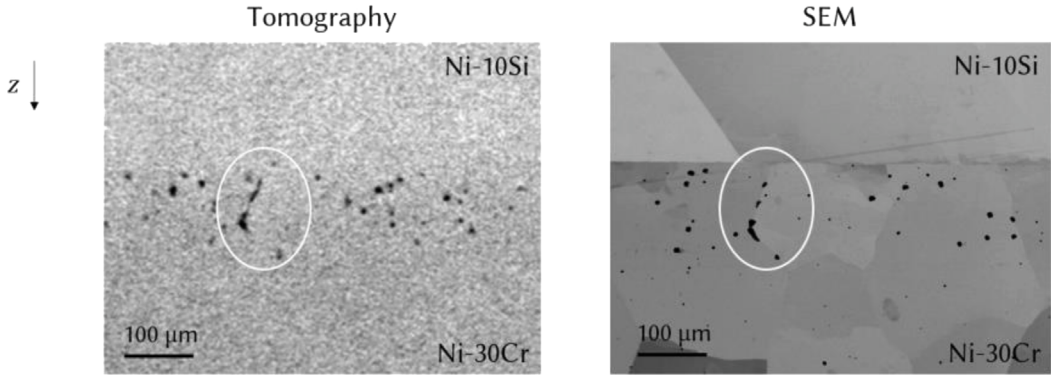

Fig. 7. Images obtained by X-ray tomography and SEM (BSE) of the same zone in a Ni–30Cr/Ni–10Si couple after a 19 h diffusion test at 1176 °C, showing elongated pores along grain boundaries. Couple prepared from an as-homogenized Ni–30Cr alloy.

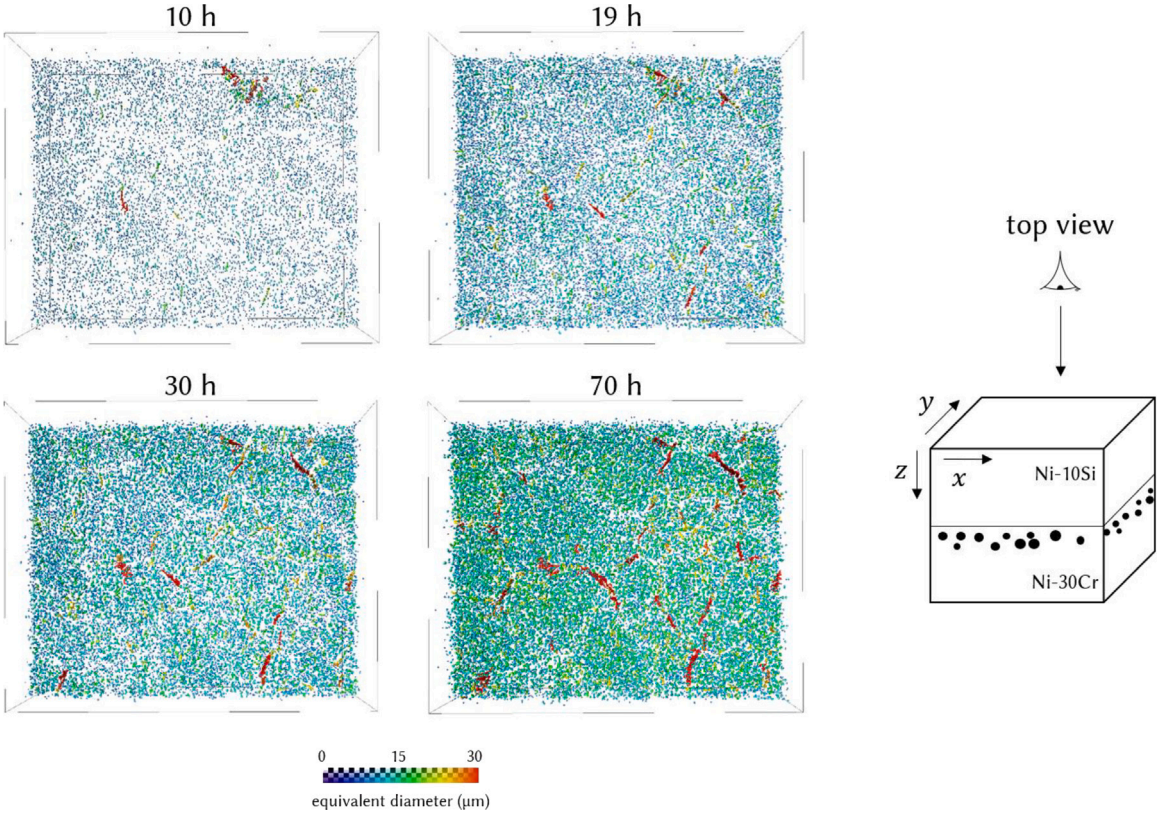

Fig. 8. Top view reconstruction of porosity in a Ni–30Cr/Ni–10Si couple during an interrupted diffusion test at 1176 °C. The pores are colored according to their equivalent diameter. The couple was prepared from a fine-grained Ni–30Cr alloy (Table 1). (For interpretation of the references to color in this figure legend, the reader is referred to the web version of this article.)

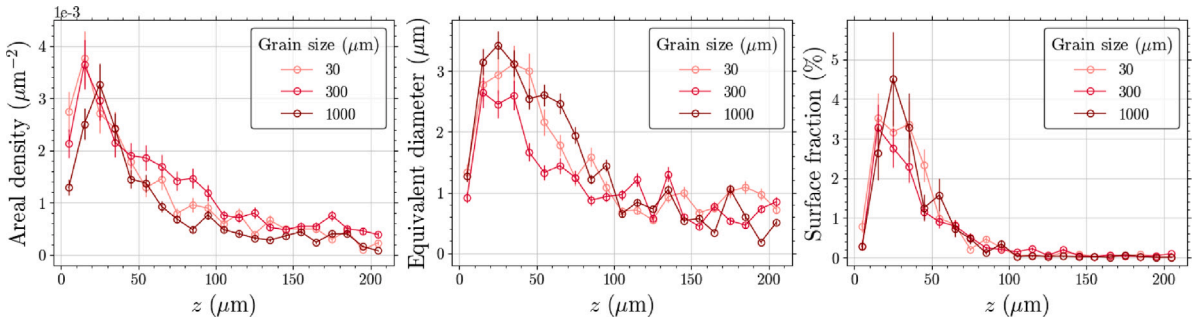

Fig. 9. Porosity distribution (areal number density, equivalent diameter, surface fraction) in Ni–30Cr/Ni–10Si couples prepared from Ni–30Cr alloys with different initial grain sizes (Table 1), after a 10 h diffusion test at 1176 °C. Data from optical micrographs, plotted against the distance to the Kirkendall plane, on the Ni–30Cr side.

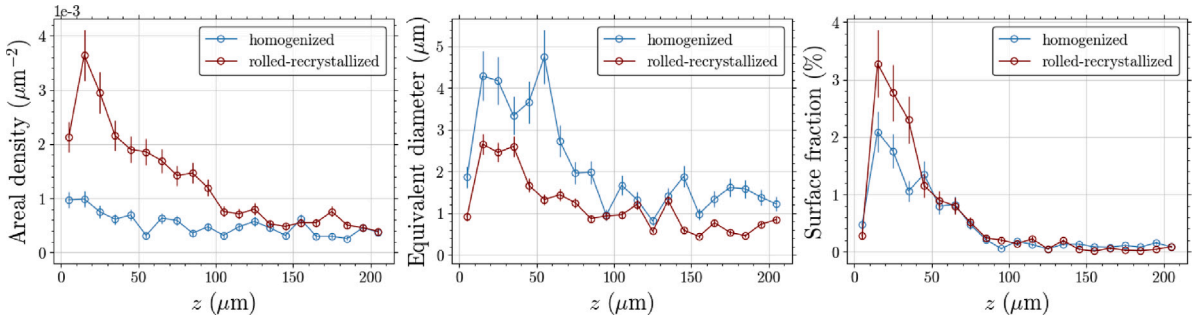

Fig. 10. Porosity distribution (areal number density, equivalent diameter, surface fraction) in Ni–30Cr/Ni–10Si couples prepared with Ni–30Cr alloys that were either homogenized or cold-rolled and recrystallized, with mm-large grains in both cases, after a 10 h diffusion test at 1176 °C. Data from optical micrographs, plotted against the distance to the Kirkendall plane, on the Ni–30Cr side.

Part of the dislocations introduced by cold rolling may subsist after the recrystallization heat treatment, despite the high annealing temperature (1176 °C). Transmission electron microscopy observations indicated that the dislocation density was locally higher in the recrystallized alloy [40] — the inhomogeneous distribution of the dislocations makes quantification difficult, see Ref. [40]. One may expect that a larger dislocation density reduces the vacancy supersaturation and therefore the pore growth, but the contrary was observed. The reason could be that the remaining dislocations are less prone to climb and consequently not very efficient as vacancy sinks. The apparent effect of cold rolling and recrystallization is therefore not due to the bulk dislocation density. Consequently, it is likely that this effect is rather related to a change in the grain boundary properties, as suggested above.

3.1.3. Discussion

Grain boundaries are commonly viewed as vacancy sinks, i.e., the sink strength associated with grain boundaries is larger than that of the bulk crystal. In irradiated materials, this tends to produce void-free zones in the vicinity of grain boundaries, where the vacancy concentration has dropped below the critical value required to form pores [39]. One possible way in which grain boundaries annihilate vacancies is by forming pores, and indeed, grain boundaries are often found to be decorated with pores in irradiated materials [39]. In the present work, the analysis of pore distribution suggests that pore growth is faster along grain boundaries than in the bulk crystal. This is possibly related to the interface energy associated with grain boundaries, which makes increasing a pore surface area more favorable than in the bulk crystal. Fast diffusion along grain boundaries may also contribute to increasing the amount of vacancies fed to a pore growing on a grain boundary.

Despite this favored growth, the grain size had no visible effect on the global pore fraction, possibly because the smallest grain size used here was still too high. Overall, pore formation in the grain interior was a prevailing mechanism of vacancy annihilation. The present observations of the Kirkendall effect in a diffusion couple are quite remote from the limiting case studied in theoretical works [8], where the crystal forms no pores, and the sink strength is null in the bulk crystal (causing a large vacancy supersaturation) and infinitely large on grain boundaries (maintaining the vacancies at equilibrium).

Two additional factors appeared to play an important role in pore formation. First, our results suggest that the sink strength associated with grain boundaries depend on their structure (Fig. 10), as observed by previous investigators in irradiated copper [39]. Second, the heterogeneous distribution of pores suggests that their nucleation is mainly heterogeneous, and that it is governed by factors that were not controlled in our experiments — it is possible that oxide particles present from the alloy fabrication acted as nucleation sites [52], and that these were distributed in a non-uniform manner.

3.2. Time evolution

We now examine the time evolution of the porosity. Fig. 11 represents profiles obtained by optical microscopy from separate samples. As time progresses, the maximum pore fraction increases, because of an increase of both their density and size. Furthermore, the position of the porosity peak is shifted toward the bulk of the Ni–30Cr alloy. This shift is accompanied by a decrease of the pore size and surface fraction close to the interface, visible on the profiles and on the micrographs. This raises the following question: does the pore population evolve through the movement of individual pores, or by a growth-shrinkage sequence of immobile pores?

This question is examined using tomography data obtained from an interrupted test. Fig. 12 presents the 3D reconstruction of the pores detected between 10 and 70 h,[1] and the number density, equivalent diameter and volume fraction profiles. These are consistent with the main features observed by optical microscopy. The decrease of the pore fraction close to the interface is not observed by tomography, most likely because the pores initially formed in this zone were too small to be detected. However, the tomography data reveal a separation between two zones with distinct pore distributions: close to the initial interface (0–40 μm), the pores are smaller and more densely packed, and their density initially increases (up to 19 h), then decreases; beyond 40 μm, the density and size increase over time.

The pore coordinates were processed to track pore displacements from one interruption time to the next. The results are summarized in Fig. 13. The top row shows the displacement in the diffusion direction (Δz), as a function of position on the same axis, between the test interruptions. The black dots represent binned data. The colored dots represent individual pores: the equivalent diameter and its relative variation from one time to the next are mapped to the dot size and color, respectively. The bottom row shows the displacements along the two other space axes between 30 h and 70 h. The following observations can be made:

- The data are very noisy: at a given position, numerous pores move toward the initial interface ($\Delta z < 0$) and toward the bulk of the Ni–30Cr alloy ($\Delta z > 0$). Furthermore, the absolute Δz values are small relative to the voxel size (1.9 μm).
- Nevertheless, a trend is visible: pores closest to the interface tend to move toward the bulk, while those further away tend to move toward the interface. The Δx and Δy values are comparable to those of Δz, but appear to be randomly distributed along z. This suggests that the trend observed for Δz is significant.
- The pores that are closest to the interface tend to shrink over time, while those further away grow.

[1] A first analysis was done after 2 h, but the majority of pores were too small to be detected by tomography.

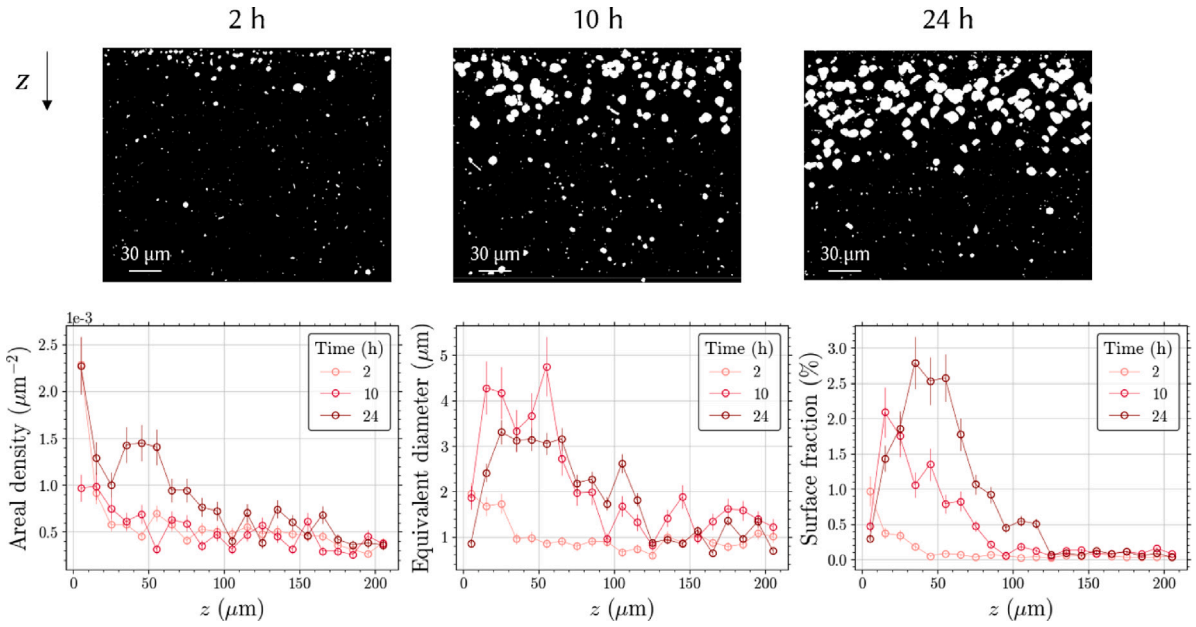

Fig. 11. Time evolution of the porosity in Ni–30Cr/Ni–10Si couples after diffusion tests at 1176 °C, analyzed by optical microscopy. Top: superposition of thresholded, binarized images (pores in white, alloy in black) showing all pores observed on a cross-section, in the Ni–30Cr alloy (the Kirkendall plane is on the image top borders). Bottom: areal number density, equivalent diameter and surface fraction against the distance to the Kirkendall plane, on the Ni–30Cr side. Couples prepared from an as-homogenized Ni–30Cr alloy.

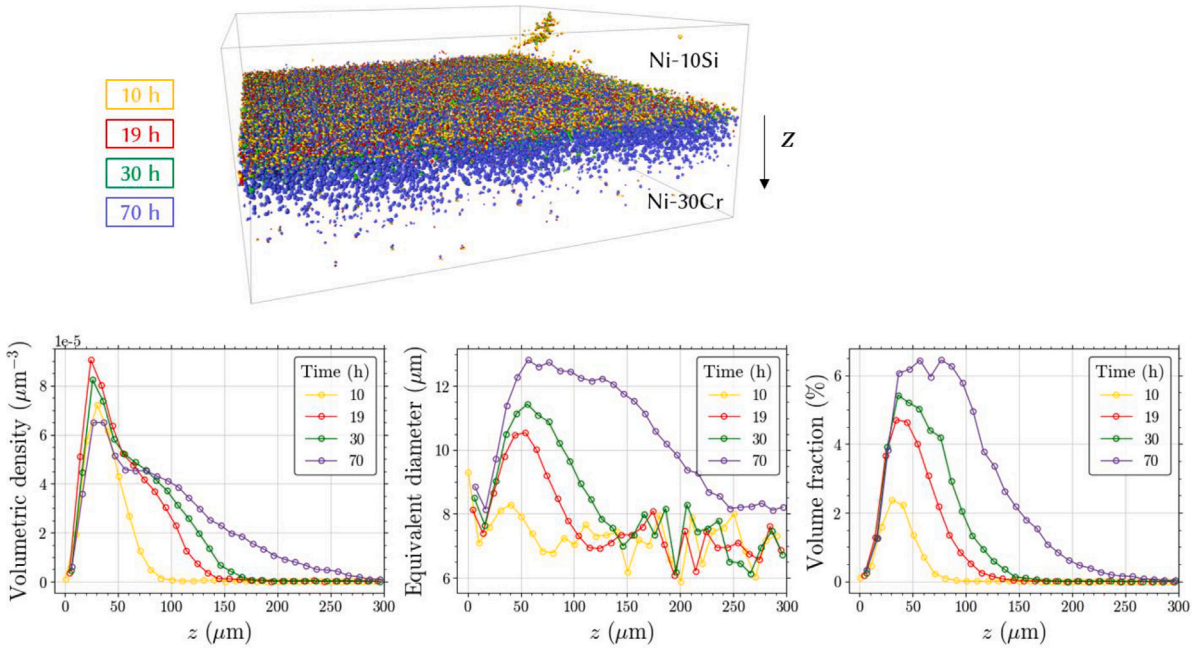

Fig. 12. Time evolution of the porosity in Ni–30Cr/Ni–10Si couples after diffusion tests at 1176 °C, analyzed by tomography. Top: Pore reconstruction, colored by diffusion time. Bottom: volumetric number density, equivalent diameter and volume fraction against the distance to the Kirkendall plane, on the Ni–30Cr side. Couples prepared from a fine-grained Ni–30Cr alloy (Table 1). (For interpretation of the references to color in this figure legend, the reader is referred to the web version of this article.)

These observations are consistent with the global analysis presented in Fig. 12. Both sets of results suggest that the porosity evolves through both pore movement and a growth-shrinkage sequence. These mechanisms do not operate uniformly: close to the interface, both the pore movement and the growth-shrinkage sequence contribute to a shift of the pore population toward the bulk of the Ni–30Cr alloy, whereas farther in the Ni–30Cr alloy, the pore movement opposes the growth-shrinkage sequence, and the latter prevails to produce an overall shift toward the bulk.

The Kirkendall porosity develops in vacancy supersaturation zones, i.e., in zones where the divergence of the vacancy flux is negative — in 1D, $\frac{\partial J_{Va}}{\partial z} < 0$. The shape of the vacancy flux profile is difficult to anticipate in a ternary system,[2] and is more conveniently studied from simulations. Fig. 14 presents profiles of the vacancy flux (J_{Va}) and its divergence ($\frac{\partial J_{Va}}{\partial z}$) obtained from a simulation of a Ni–30Cr/Ni–10Si

[2] In the usual sense: three chemical elements plus vacancies.

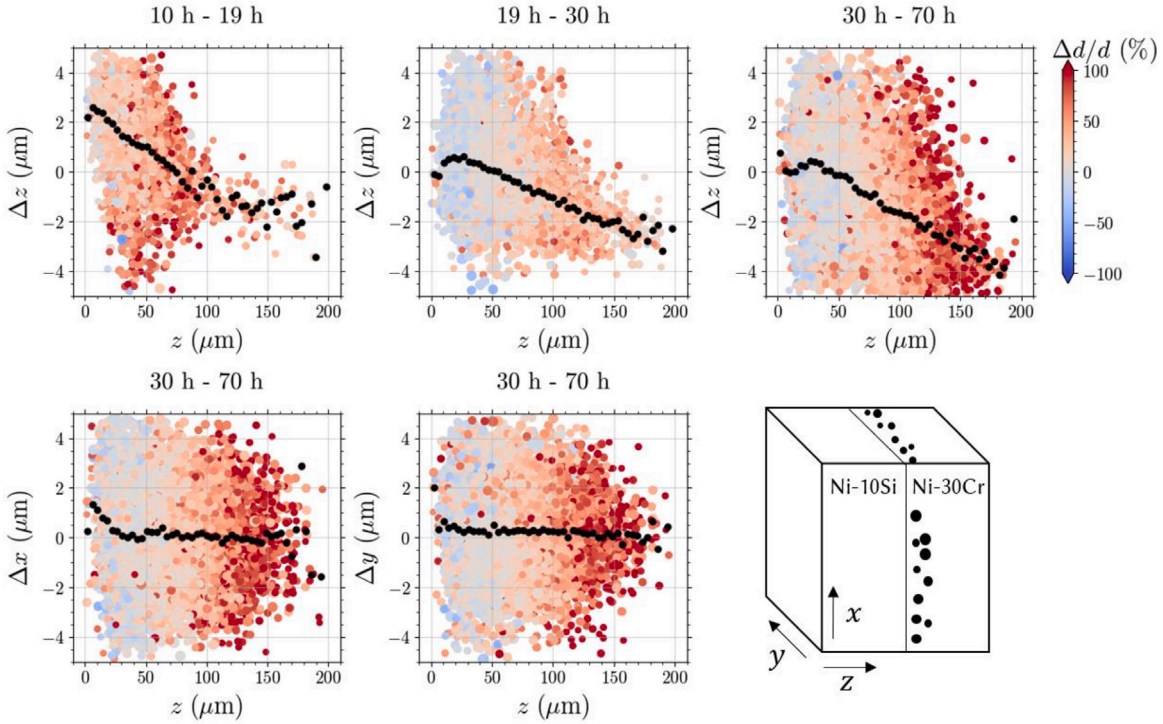

Fig. 13. Pore displacement over time as a function of their position in a Ni–30Cr/Ni–10Si couple during diffusion at 1176 °C, obtained from the tomography data shown in Fig. 12. Top: displacement in the diffusion direction, z. The position $z = 0$ corresponds to the Kirkendall plane; positive Δz values correspond to displacements toward the bulk of the Ni–30Cr alloy. Bottom: displacements in the x and y directions between 30 and 70 h. The black dots represent binned data, while the colored dots represent individual pores. For the latter, the dot size is proportional to the pore size, and the color represents the relative variation of equivalent diameter in the considered time interval. (For interpretation of the references to color in this figure legend, the reader is referred to the web version of this article.)

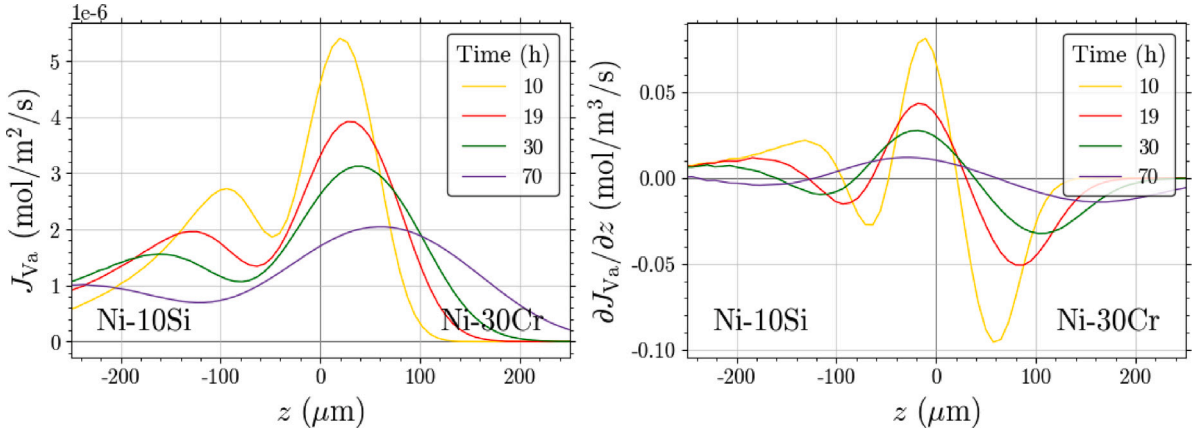

Fig. 14. Simulated profiles of the vacancy flux and its divergence in a Ni–30Cr/Ni–10Si couple during diffusion at 1176 °C. The position $z = 0$ represents the initial interface. Simulation done with our mobility data (see Table 2), in the ideal lattice hypothesis.

couple at 1176 °C, at the times corresponding to the tomography data. The following observations can be made:

- On the Ni–30Cr side, close to the initial interface ($z < 20$ μm), the divergence is positive: this indicates an undersaturation zone, where pores are expected to act as vacancy sources, i.e., to shrink to provide vacancies to the crystal.[3]
- Between $z = 20$ and 40 μm, the divergence is negative at 10 h (supersaturation, pore growth) then becomes positive (undersaturation, pore shrinkage).
- Further away ($z > 40$ μm), the divergence is negative (supersaturation, pore growth), with a peak that shifts toward the bulk of the Ni–30Cr alloy as time progresses.
- On the left of the peak, the slope of the divergence is negative: the driving force for pore growth is more important on the bulk side than on the interface side. At the scale of an individual pore, this difference is expected to cause faster growth on the bulk side,

[3] For shorter diffusion times, the divergence is strongly negative in this zone, which causes the initial pore growth.

which would generate a net displacement toward the bulk. On the contrary, on the right of the minimum, the slope is positive: the driving force for pore growth is more intense on the interface side than on the bulk side, which would lead to pore displacement toward the interface.

As shown in Section 2.2, the simulation results are sensitive to the input data, and only offer an approximate representation of the experimental reality. Nevertheless, the time evolution of the pore distribution observed experimentally is generally consistent with that of the simulated vacancy flux. Pores first develop with a high density close to the interface, where the divergence of the vacancy flux is strongly negative, then shrink as the negative vacancy divergence zone shifts toward the bulk of the Ni–30Cr alloy. Meanwhile, new pores nucleate further and further away in the Ni–30Cr alloy, and grow larger. Pores located on the interface side of the negative vacancy divergence peak tend to move toward the bulk, while those located on the bulk side of the negative vacancy divergence peak tend to move toward the interface, opposing the growth-shrinkage sequence. The latter prevails, and the pore population shifts toward the bulk.

4. Conclusions

From a methodological standpoint, our work demonstrates the advantages and disadvantages of cross-sectional microscopy and tomography to study the Kirkendall porosity. In our experimental conditions, optical microscopy provided a better spatial resolution than X-ray tomography with a micrometer-range laboratory device (0.2 μm/pixel vs. 1.9 μm/pixel). The latter offered a much larger sample size, and therefore a better representation of the pore population. The two techniques yielded similar estimations of pore fraction profiles. X-ray tomography additionally allowed monitoring the time evolution of the porosity in a given couple. This was used to track the position and size of thousands of pores over tens of hours through an interrupted diffusion test. The amplitude of pore displacements was close to the measurement resolution: using a high resolution nanofocus X-ray tube or synchrotron radiation instead of a microfocus laboratory source would be useful to refine the trends observed here.

With regard to predicting the porosity through multicomponent diffusion simulation, we showed that the calculated porosity profiles were very sensitive to the input mobility data, in particular, much more sensitive than the concentration profiles were.

The local analysis of the porosity showed that pore nucleation was not significantly accelerated on grain boundaries compared to the grain interior, but that pores grew faster along grain boundaries. However, the initial alloy grain size had no visible effect on the overall pore distribution, likely because the contrast between pore development on grain boundaries and in the grain interior was not strong enough given the grain sizes that were explored (30 μm to 1 mm). Smaller grain sizes may produce visibly different results if they can be stabilized during the diffusion experiment — grain growth tends to be very rapid at the temperatures of interest.

The time-resolved pore distribution data indicated that the porosity developed through both individual pore movement and a growth-shrinkage sequence. These mechanisms operate across the interdiffusion zone in accordance with the vacancy flux profile. Pores start developing close to the interface, where the divergence of the vacancy flux is most negative. As diffusion proceeds, the negative vacancy divergence zone shifts toward the bulk of the Ni–30Cr alloy. The initial pores shrink and disappear, while new pores nucleate and grow further and further away in the alloy. The pores also tend to move toward the peak of the vacancy divergence. Overall, the growth-shrinkage sequence prevails, causing a shift of the pore population toward the bulk.

CRediT authorship contribution statement

Camille Salsi: Formal analysis, Investigation, Methodology, Visualization, Writing – original draft. **Julien Lesseur:** Formal analysis, Investigation, Methodology, Visualization, Writing – review & editing. **Daniel Monceau:** Conceptualization, Methodology, Writing – review & editing. **Clara Desgranges:** Conceptualization, Methodology, Writing – review & editing. **Thomas Gheno:** Conceptualization, Formal analysis, Funding acquisition, Methodology, Visualization, Writing – original draft, Writing – review & editing.

Funding

This work was supported by the Agence Nationale de la Recherche, France, grant number ANR-19-CE08-0004.

Declaration of competing interest

The authors declare that they have no known competing financial interests or personal relationships that could have appeared to influence the work reported in this paper.

Acknowledgments

The authors thank Cédric Lopes and Catherine Rio at ONERA for producing the ingots and helping with SEM analyses, respectively, and Loic Perrière at ICMPE for cold rolling the ingots.

Appendix A. Geometrical relationships between a population of spherical pores and the disks observed on a cross-section[4]

We seek to compare the morphological properties (radius, surface/volume fraction, areal/volumetric number density) of a set of pores from measurements in 3D and on a cross-section. To do so, we compute the properties of random sets of spherical pores.

In each draw, we consider a set of pores whose centers of coordinates $c_i = (x_i, y_i, z_i)$ are contained in a cubic domain of side L. Without loss of generality, we suppose that the cross-section plane P is normal to the x axis ($P : x = x_P$, see Fig. A.1a). The draw proceeds as follows:

- A number of pores n is drawn on a discrete uniform distribution with bounds $n_{\min}$ and $n_{\max}$.
- The abscissas of the pore centers, x_i, are drawn on a uniform distribution ($x \in [0, L]$).[5]
- The pore radii, R_i, are drawn on a lognormal distribution with parameters μ and σ: $\ln R \sim \mathcal{N}(\mu, \sigma^2)$.
- The abscissa of the cutting plane, x_P, is drawn on a uniform distribution ($x_P \in [0, L]$).

The distance between the pore centers and the cutting plane is:

$$\rho_i = |x_i - x_P| . \tag{A.1}$$

We consider the m pores whose intersection with the cutting plane is not empty, defined by $\rho_i < R_i$. The radius of the disk at the intersection of a pore and the plane is given by (see Fig. A.1b)[6]:

$$r_i = \sqrt{R_i^2 - \rho_i^2}. \tag{A.2}$$

[4] Adapted from text published in French in Ref. [41].

[5] Since the cutting plane is normal to the x axis, the coordinates y_i and z_i have no influence on the results.

[6] For the more general case where the cutting plane is not oriented in any particular way, the reader is directed to Ref. [53], which we have drawn upon here.

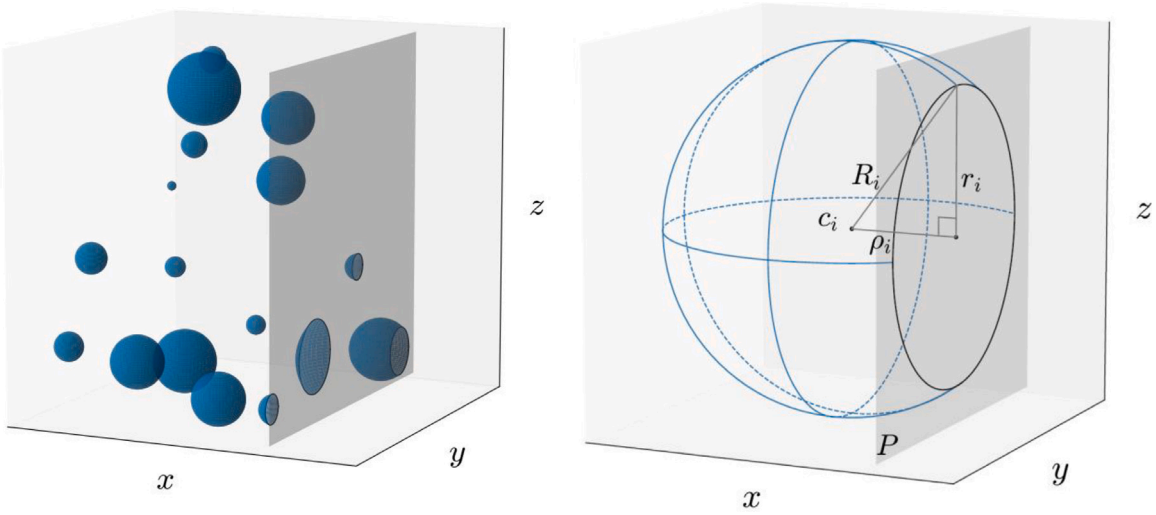

Fig. A.1. Spherical pores and cross-section plane. (a) Pore population. (b) Variables used to calculate the radius of the disk at the intersection between the pore and the cutting plane. Inspired from Ref. [53] and reproduced from Ref. [41].

The volume fraction of pores is[7]:

$$f_V = \sum_{i=1}^{n} f_V^i = \frac{1}{L^3}\frac{4}{3}\pi \sum_{i=1}^{n} R_i^3, \tag{A.3}$$

while the surface fraction of the disks measured on the cutting plane is:

$$f_S = \sum_{i=1}^{m} f_S^i = \frac{1}{L^2}\pi \sum_{i=1}^{m} r_i^2. \tag{A.4}$$

The volumetric number density of pores is:

$$n_V = \frac{n}{L^3}, \tag{A.5}$$

while the areal number density of disks on the cutting plane is:

$$n_S = \frac{m}{L^2}. \tag{A.6}$$

We note $\bar{R}_j$ the mean of the R_{ij} pore radii obtained during draw j:

$$\bar{R}_j = \frac{1}{n}\sum_{i=1}^{n} R_{ij}, \tag{A.7}$$

and $\bar{\bar{R}}$ the mean value obtained over N draws:

$$\bar{\bar{R}} = \frac{1}{N}\sum_{j=1}^{N} \bar{R}_j. \tag{A.8}$$

The same notations are used for the disk radii r_{ij}.

The computations were done with a domain of side $L = 1$ mm, a pore number comprised between $n_{\min} = 5^3 = 125$ and $n_{\max} = 32^3 = 32\,768$, an expected pore radius $\mu_R = 5$ µm and a standard deviation $\sigma_R = 2.5$ µm. The parameters of the lognormal pore radius distribution are related to μ_R and σ_R via

$$\mu = \ln\left(\frac{\mu_R^2}{\sqrt{\mu_R^2 + \sigma_R^2}}\right), \tag{A.9}$$

$$\sigma^2 = \ln\left(1 + \frac{\sigma_R^2}{\mu_R^2}\right). \tag{A.10}$$

The parameters were chosen so as to obtain results consistent with the experimental results, i.e., volume fractions between 0 and 3%.

[7] Some pores may extend over the domain boundaries. It follows that the value computed by Eq. (A.3) is overestimated. However, the conditions are chosen so that $R_i \ll L \ \ \forall i$; the error is therefore insignificant.

Fig. A.2 presents the results obtained after $N = 10^4$ draws. The set of mean disk radii $\bar{r}$ is relatively scattered, but centered around the expected radius $\mu_R = 5$ µm: we obtain $\bar{\bar{r}} = 4.91$ µm (Fig. A.2a). In many draws, the mean disk radius $\bar{r}_j$ is larger than the mean pore radius $\bar{R}_j$: this may seem unexpected inasmuch as the radius of a disk is necessarily smaller than or equal to that of the pore being cut. This is due to the fact that larger pores are more likely to be contained in the cutting plane. Indeed, we verify that when the standard deviation σ decreases, the dispersion of the $\bar{r}_j$ values and the overall mean $\bar{\bar{r}}$ decrease as well — in the extreme case where $\sigma = 0$, i.e., all pores have the same radius $R_{ij} = \mu_R = 5$ µm, we observe that $\bar{r}_j < \mu_R \ \forall j$ and obtain $\bar{\bar{r}} = 3.93$ µm.

Fig. A.2b shows that the surface fractions f_S are quite close to the volume fractions f_V. This stems from two antagonistic biases: on the one hand, the surface fraction of the cutting plane occupied by a disk is much larger than the volume fraction occupied by the pore being cut:

$$f_S^i \gg f_V^i, \ \textit{i.e.}, \quad \pi\frac{r_i^2}{L^2} \gg \frac{4}{3}\pi\frac{R_i^3}{L^3} \quad \forall i, \tag{A.11}$$

since $R_i \ll L \ \forall i$; on the other hand, the number of disks on a cutting plane is much smaller than the number of pores in the domain: $m \ll n$. Specifically, we can show (Fig. A.2c) that $n_S \approx 2\bar{R}n_V$, which implies, using Eqs. (A.5) and (A.6),

$$m \approx n\frac{2\bar{R}}{L}. \tag{A.12}$$

Appendix B. Optimization of mobility parameters

The mobility parameters were optimized using an in-house software called Optimob, whose principle is illustrated in Fig. B.1 and can be summarized as follows.[8] The description of atomic mobility relies on the Calphad method [54,55]. The temperature dependence of the tracer diffusion coefficients is described with an Arrhenius law:

$$D_k^* = D_k^0 \exp\left(-\frac{Q_k}{RT}\right), \tag{B.1}$$

where D_k^0 are the preexponential factors, Q_k the activation energy, R the ideal gas constant and T the temperature. This can also be written:

$$\ln D_k^* = \frac{\phi_k}{RT}, \tag{B.2}$$

[8] Adapted from text published in French in Ref. [41].

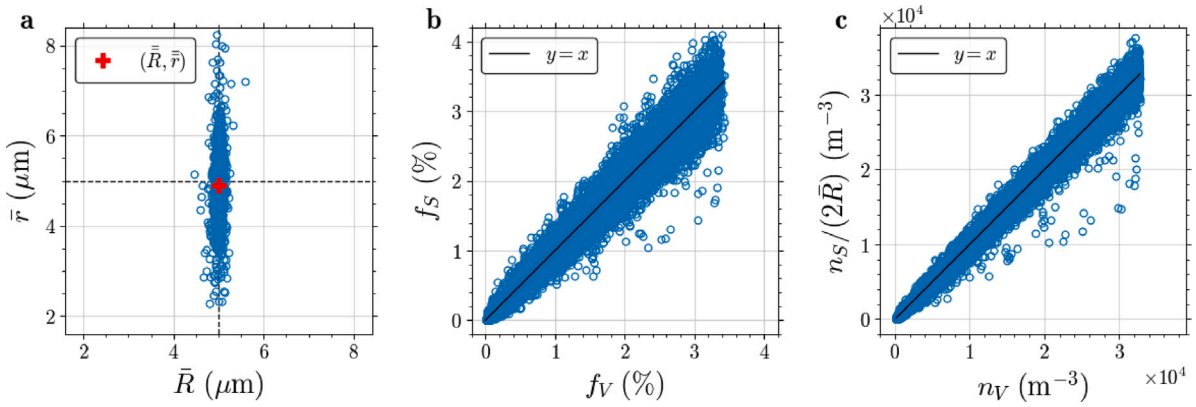

Fig. A.2. Properties computed from 10^4 sets of pores, with the parameters given in the text, in the volume and in a random cutting plane. (a) Mean disk radius measured on the cutting plane, as a function of the mean pore radius; (b) surface fraction of the disks on the cutting plane as a function of the pore volume fraction; (c) ratio of the areal number density over the mean pore diameter, as a function of the volume number density.

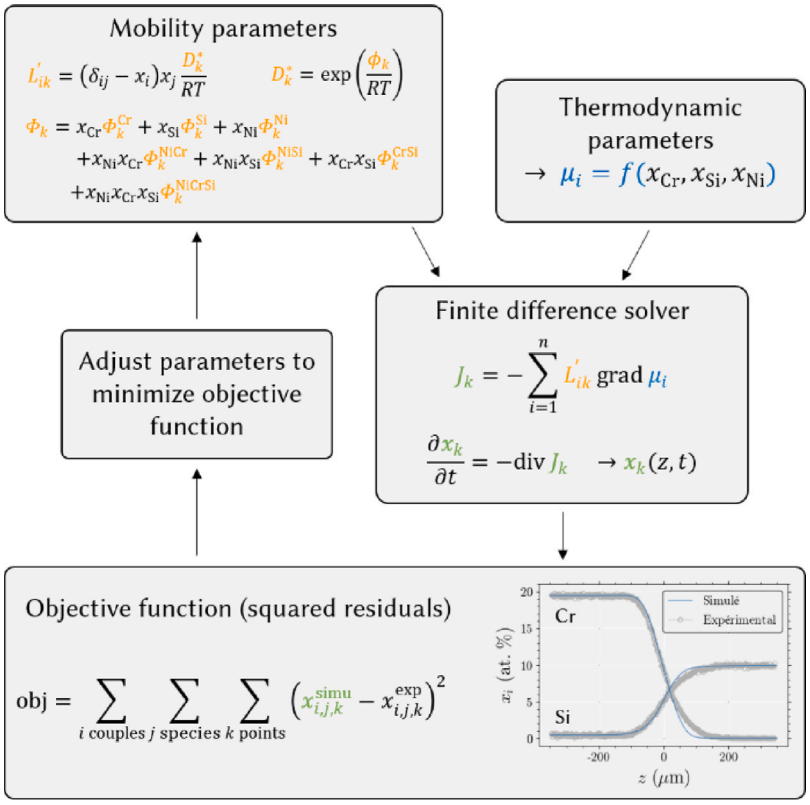

Fig. B.1. Procedure of mobility parameter optimization from experimental concentration profiles.
Source: Adapted from Ref. [41]

with $\phi_k = RT \ln D_k^0 - Q_k$. The composition dependence of the ϕ_k is modeled using Redlich–Kister polynomials, with binary and ternary interactions of order 0:

$$\begin{aligned}\phi_k = {} & x_{Cr}\phi_k^{Cr} + x_{Si}\phi_k^{Si} + x_{Ni}\phi_k^{Ni} \\ & + x_{Ni}x_{Cr}\phi_k^{NiCr} + x_{Ni}x_{Si}\phi_k^{NiSi} + x_{Cr}x_{Si}\phi_k^{CrSi} \\ & + x_{Ni}x_{Cr}x_{Si}\phi_k^{NiCrSi}\end{aligned} \tag{B.3}$$

The ϕ_k^i, ϕ_k^{ij} and ϕ_k^{ijk} are the mobility parameters. The ternary system Ni–Cr–Si is described by 21 parameters (9 unary, 9 binary and 3 ternary). In general, these parameters vary with temperature and are stored in the form $A + BT$; in the present case, however, the optimization was performed at a single temperature (1176 °C): their temperature dependence was not determined.

To avoid overfitting, each parameter should be optimized using experimental data that are sufficiently sensitive to it. This general principal was declined to reduce the number of parameters to be optimized, which led to the following procedure:

- The unary terms selected by Du and Schuster [46] were retained here.
- The Cr–Si binary does not have a fcc phase, and the mobilities in the Ni-rich zone of the Ni-Cr-Si ternary are little sensitive to the ϕ_k^{CrSi} terms. These were set to 0, as is customary.

- The ϕ_{Cr}^{CrNi} and ϕ_{Ni}^{CrNi} terms were optimized using profiles measured in a binary Ni/Ni–30Cr couple. Similarly, the ϕ_{Si}^{NiSi} and ϕ_{Ni}^{NiSi} terms were optimized using profiles measured in a binary Ni/Ni–10Si couple.
- The other binary terms and the ternary terms were optimized from the following ternary couples: Ni–30Cr/Ni–10Si, Ni–30Cr/Ni–10Cr–10Si, Ni–30Cr/Ni–20Cr–10Si, Ni–20Cr/Ni–10Si, Ni–20Cr/Ni–10Cr–10Si and Ni–20Cr/Ni–20Cr–10Si.

The optimization is conducted in successive steps, where the experimental profiles to consider and the parameters to optimize are selected. At each step, the optimization is run by an inverse numerical method inspired from Campbell [56]. A finite difference solver is used to compute the profiles of the selected couples. The underlying diffusion model assumes vacancies remain at equilibrium and neglects the effect of non-equilibrium vacancies and porosity on the composition profiles (“ideal lattice” hypothesis, see main text). This is justified inasmuch as these effects are indeed small [37] relative to experimental scatter. The parameters are then adjusted to minimize the squared difference between the experimental and computed profiles. The initial estimates of the parameters are the values from Du and Schuster [46]. The optimized parameters are given in Ref. [40].

The profiles computed with the Du and Schuster database [46] and our database are compared with the experimental profiles in Fig. 5 in the case of the Ni–30Cr/Ni–10Si couple. Equivalent graphs for all the other couples are provided in Refs. [40,41]. The agreement between the computed and experimental profiles is consistently better with our database. This is due to the fact that the experimental profiles are precisely those used in the optimization; it does not mean that our database offers a better description of atomic mobilities in the fcc phase of the Ni–Cr–Si system in general. Indeed, the Du and Schuster database [46] was obtained based on a critical assessment of experimental data at multiple temperatures from multiple sources, whereas our database is specifically adapted to reproduce our data set.

References

[1] J.R. Nicholls, Advances in coating design for high-performance gas turbines, MRS Bull. 28 (2003) 659–670, http://dx.doi.org/10.1557/mrs2003.194.

[2] M.P. Bacos, J.M. Dorvaux, O. Lavigne, R. Mévrel, M. Poulain, C. Rio, M.H. Vidal-Sétif, Performance and degradation mechanisms of thermal barrier coatings for turbine blades: a review of ONERA activities, AerospaceLab (2011) 1–11.

[3] D.R. Clarke, M. Oechsner, N.P. Padture, Thermal-barrier coatings for more efficient gas-turbine engines, Mrs Bull. 37 (2012) 891–902, http://dx.doi.org/10.1557/mrs.2012.232.

[4] D. Texier, D. Monceau, S. Selezneff, A. Longuet, E. Andrieu, High temperature micromechanical behavior of a pt-modified nickel aluminide bond-coating and of its interdiffusion zone with the superalloy substrate, Met. Mat Trans A (2020) http://dx.doi.org/10.1007/s11661-020-05634-2.

[5] E.O. Kirkendall, Diffusion of zinc in alpha brass, in: Transactions of the AIME, 1942, pp. 104–110.

[6] A.D. Smigelskas, E.O. Kirkendall, Zinc diffusion in alpha brass, in: Transactions of the AIME, 1947, pp. 130–142.

[7] H. Nakajima, The discovery and acceptance of the kirkendall effect: The result of a short research career, JOM 49 (1997) 15–19, http://dx.doi.org/10.1007/BF02914706.

[8] A. Van der Ven, H.-C. Yu, G. Ceder, K. Thornton, Vacancy mediated substitutional diffusion in binary crystalline solids, Prog. Mater. Sci. 55 (2010) 61–105, http://dx.doi.org/10.1016/j.pmatsci.2009.08.001.

[9] G.B. Stephenson, Deformation during interdiffusion, Acta Metall. 36 (1988) 2663–2683, http://dx.doi.org/10.1016/0001-6160(88)90114-9.

[10] J.A. Dantzig, W.J. Boettinger, J.A. Warren, G.B. McFadden, S.R. Coriell, R.F. Sekerka, Numerical modeling of diffusion-induced deformation, Met. Mat Trans A 37 (2006) 2701–2714, http://dx.doi.org/10.1007/BF02586104.

[11] H.-C. Yu, A.V. der Ven, K. Thornton, Simulations of the Kirkendall-effect-induced deformation of thermodynamically ideal binary diffusion couples with general geometries, Met. Mat Trans A 43 (2012) 3481–3500, http://dx.doi.org/10.1007/s11661-012-1299-x.

[12] A. Gusak, B. Wierzba, M. Danielewski, Competition between Kirkendall shift and backstress in interdiffusion revisited – simple analytic model, Phil. Mag. 94 (2014) 1153–1165, http://dx.doi.org/10.1080/14786435.2013.878053.

[13] F.D. Fischer, J. Svoboda, Stress deformation and diffusion interactions in solids – a simulation study, J. Mech. Phys. Solids 78 (2015) 427–442, http://dx.doi.org/10.1016/j.jmps.2015.02.018.

[14] F. Seitz, On the porosity observed in the Kirkendall effect, Acta Metall. 1 (1953) 355–369, http://dx.doi.org/10.1016/0001-6160(53)90112-6.

[15] R.W. Balluffi, The supersaturation and precipitation of vacancies during diffusion, Acta Metall. 2 (1954) 194–202, http://dx.doi.org/10.1016/0001-6160(54)90159-5.

[16] K. Kasai, H. Murakami, K. Noda, Effect of thermal history on microstructural changes in aluminized nickel-based single-crystal superalloy, Mater. Trans. 54 (2013) 2252–2257, http://dx.doi.org/10.2320/matertrans.M2013205.

[17] B. Wierzba, W. Skibiński, The interdiffusion in copper-nickel alloys, J. Alloys Compd. 687 (2016) 104–108, http://dx.doi.org/10.1016/j.jallcom.2016.06.085.

[18] F.J.J. van Loo, B. Pieraggi, R.A. Rapp, Interface migration and the kirkendall effect in diffusion-driven phase transformations, Acta Met. et Mater. 38 (1990) 1769–1779, http://dx.doi.org/10.1016/0956-7151(90)90019-D.

[19] R. Voigt, V. Ruth, The development of surface contour changes during interdiffusion in silver/gold alloy diffusion couples, J. Phys.: Condens. Matter. 7 (1995) 2655–2666, http://dx.doi.org/10.1088/0953-8984/7/14/006.

[20] I. Daruka, I.A. Szabo, D.L. Beke, Cs. Cserhati, A. Kodentsov, F.J.J. van Loo, Diffusion-induced bending of thin sheet couples: Theory and experiments in Ti-Zr system, Acta Mater. 44 (1996) 4981–4993, http://dx.doi.org/10.1016/S1359-6454(96)00099-7.

[21] E. Schulz, A. Mehta, S.H. Park, Y. Sohn, Effects of marker size and distribution on the development of kirkendall voids, and coefficients of interdiffusion and intrinsic diffusion, J. Phase Equilib. Diffus. 40 (2019) 156–169, http://dx.doi.org/10.1007/s11669-019-00710-6.

[22] M.J.H. van Dal, M.C.L.P. Pleumeekers, A.A. Kodentsov, F.J.J. van Loo, Intrinsic diffusion and kirkendall effect in ni–pd and fe–pd solid solutions, Acta Mater. 48 (2000) 385–396, http://dx.doi.org/10.1016/S1359-6454(99)00375-4.

[23] A. Paul, M.J.H. van Dal, A.A. Kodentsov, F.J.J. van Loo, The kirkendall effect in multiphase diffusion, Acta Mater. 52 (2004) 623–630, http://dx.doi.org/10.1016/j.actamat.2003.10.007.

[24] P. Audigié, A. Rouaix-Vande Put, A. Malié, P. Bilhé, S. Hamadi, D. Monceau, Observation and modeling of α-niptal and kirkendall void formations during interdiffusion of a pt coating with a γ-(Ni-13al) alloy at high temperature, Surf. Coat. Technol. 260 (2014) 9–16, http://dx.doi.org/10.1016/j.surfcoat.2014.08.083.

[25] A. Epishin, B. Camin, L. Hansen, A. Chyrkin, G. Nolze, Synchrotron sub-μ X-ray tomography of kirkendall porosity in a diffusion couple of nickel-base superalloy and nickel after annealing at 1250 °c, Adv. Eng. Mater. 23 (2021) 2001220, http://dx.doi.org/10.1002/adem.202001220.

[26] P. Audigié, A. Vande Put, B. Malard, A. Malié, D. Monceau, Analysis of void formation in pt-rich γ-γ’ bond-coatings for TBC system application, Corros. Sci. 249 (2025) 112785, http://dx.doi.org/10.1016/j.corsci.2025.112785.

[27] K.P. Gurov, A.M. Gusak, Description of the interdiffusion in alloys with an arbitrary power of vacancy sinks, Fiz. Met. I Met. 59 (1985) 1062–1066.

[28] G. Martin, C. Desgranges, Diffusion in crystals with nonconservative defects, Eur. Lett. (EPL) 44 (1998) 150–155, http://dx.doi.org/10.1209/epl/i1998-00449-1.

[29] I.V. Belova, G.E. Murch, Analysis of vacancies produced at non-equilibrium concentrations by interdiffusion, Phil. Mag. 85 (2005) 1191–1203, http://dx.doi.org/10.1080/14786430412331331998.

[30] H.-C. Yu, D.-H. Yeon, A. Van der Ven, K. Thornton, Substitutional diffusion and kirkendall effect in binary crystalline solids containing discrete vacancy sources and sinks, Acta Mater. 55 (2007) 6690–6704, http://dx.doi.org/10.1016/j.actamat.2007.08.031.

[31] K.R. Elder, K. Thornton, J.J. Hoyt, The Kirkendall effect in the phase field crystal model, Phil. Mag. 91 (2011) 151–164, http://dx.doi.org/10.1080/14786435.2010.506427.

[32] A.M. Gusak, N.V. Storozhuk, Competition of K and F sinks during void formation, Phys. Met. Metallogr. 114 (2013) 197–206, http://dx.doi.org/10.1134/S0031918X13030071.

[33] F.D. Fischer, J. Svoboda, Diffusion of elements and vacancies in multi-component systems, Prog. Mater. Sci. 60 (2014) 338–367, http://dx.doi.org/10.1016/j.pmatsci.2013.09.001.

[34] B. Wierzba, Competition between Kirkendall and Frenkel effects during multi-component interdiffusion process, Phys. A 403 (2014) 29–34, http://dx.doi.org/10.1016/j.physa.2014.02.014.

[35] P. Audigié, Modélisation de l’interdiffusion et du comportement en oxydation cyclique de superalliages monocristallins à base de nickel revêtus d’une sous-couche γ-γ’ riche en platine, in: Extension Aux SystÈmes BarriÈre Thermique, Toulouse, INPT, 2015, http://www.theses.fr/2015INPT0054.

[36] C.-H. Xia, J. Kundin, I. Steinbach, S. Divinski, Model for non-equilibrium vacancy diffusion applied to study the kirkendall effect in high-entropy alloys, Acta Mater. 232 (2022) 117966, http://dx.doi.org/10.1016/j.actamat.2022.117966.

[37] T. Gheno, V. Szczepan, C. Salsi, C. Desgranges, D. Monceau, Simulation of diffusion with non-equilibrium vacancies, Kirkendall shift and porosity in single-phase alloys, Comput. Mater. Sci. 215 (2022) 111785, http://dx.doi.org/10.1016/j.commatsci.2022.111785.

[38] J. Kundin, A. Riyahi khorasgani, R. Schiedung, B. Camin, I. Steinbach, Modeling vacancy-induced porosity in compositionally-graded complex alloys, Acta Mater. 271 (2024) 119905, http://dx.doi.org/10.1016/j.actamat.2024.119905.

[39] W.Z. Han, M.J. Demkowicz, E.G. Fu, Y.Q. Wang, A. Misra, Effect of grain boundary character on sink efficiency, Acta Mater. 60 (2012) 6341–6351, http://dx.doi.org/10.1016/j.actamat.2012.08.009.

[40] C. Salsi, Etude de l'interdiffusion et de l'effet kirkendall dans les alliages métalliques à base de nickel, in: These de doctorat, Toulouse, INPT, 2023, https://www.theses.fr/2023INPT0019.

[41] T. Gheno, Contributions à l'étude de la corrosion à haute température par le dialogue essais-calculs: données, modèles, outils, HDR, Université Paris Saclay, 2024, https://hal.science/tel-04659007.

[42] C. Salsi, D. Monceau, C. Desgranges, T. Gheno, Effect of compressive creep and hydrostatic pressure on diffusion in NiCr and NiSi systems, Metall. Mater. Trans. A 53 (2022) 4247–4257, http://dx.doi.org/10.1007/s11661-022-06814-y.

[43] J. Schindelin, I. Arganda-Carreras, E. Frise, V. Kaynig, M. Longair, T. Pietzsch, S. Preibisch, C. Rueden, S. Saalfeld, B. Schmid, J.-Y. Tinevez, D.J. White, V. Hartenstein, K. Eliceiri, P. Tomancak, A. Cardona, Fiji: an open-source platform for biological-image analysis, Nat Methods 9 (2012) 676–682, http://dx.doi.org/10.1038/nmeth.2019.

[44] L.A. Feldkamp, L.C. Davis, J.W. Kress, Practical cone-beam algorithm, J. Opt. Soc. Am. A, JOSAA 1 (1984) 612–619, http://dx.doi.org/10.1364/JOSAA.1.000612.

[45] L. Höglund, J. Agren, Analysis of the kirkendall effect, marker migration and pore formation, Acta Mater. 49 (2001) 1311–1317, http://dx.doi.org/10.1016/S1359-6454(01)00054-4.

[46] Y. Du, J.C. Schuster, Assessment of diffusional mobilities of Cr, Ni, and Si in fcc cr-Ni-Si alloys, Z. Für Met. 92 (2001) 28–31.

[47] J.-O. Andersson, T. Helander, L. Höglund, P. Shi, B. Sundman, Thermo-calc & DICTRA, computational tools for materials science, Calphad 26 (2002) 273–312, http://dx.doi.org/10.1016/S0364-5916(02)00037-8.

[48] J.C. Schuster, Y. Du, Experimental investigation and thermodynamic modeling of the Cr-Ni-Si system, Metall. Mater. Trans. A 31 (2000) 1795–1803, http://dx.doi.org/10.1007/s11661-006-0248-y.

[49] C.R. Harris, K.J. Millman, S.J. van der Walt, R. Gommers, P. Virtanen, D. Cournapeau, E. Wieser, J. Taylor, S. Berg, N.J. Smith, R. Kern, M. Picus, S. Hoyer, M.H. van Kerkwijk, M. Brett, A. Haldane, J.F. del Río, M. Wiebe, P. Peterson, P. Gérard-Marchant, K. Sheppard, T. Reddy, W. Weckesser, H. Abbasi, C. Gohlke, T.E. Oliphant, Array programming with numpy, Nature 585 (2020) 357–362, http://dx.doi.org/10.1038/s41586-020-2649-2.

[50] P. Virtanen, R. Gommers, T.E. Oliphant, M. Haberland, T. Reddy, D. Cournapeau, E. Burovski, P. Peterson, W. Weckesser, J. Bright, S.J. van der Walt, M. Brett, J. Wilson, K.J. Millman, N. Mayorov, A.R.J. Nelson, E. Jones, R. Kern, E. Larson, C.J. Carey, İ. Polat, Y. Feng, E.W. Moore, J. VanderPlas, D. Laxalde, J. Perktold, R. Cimrman, I. Henriksen, E.A. Quintero, C.R. Harris, A.M. Archibald, A.H. Ribeiro, F. Pedregosa, P. van Mulbregt, SciPy 1.0 Contributors, A. Vijaykumar, A.P. Bardelli, A. Rothberg, A. Hilboll, A. Kloeckner, A. Scopatz, A. Lee, A. Rokem, C.N. Woods, C. Fulton, C. Masson, C. Häggström, C. Fitzgerald, D.A. Nicholson, D.R. Hagen, D.V. Pasechnik, E. Olivetti, E. Martin, E. Wieser, F. Silva, F. Lenders, F. Wilhelm, G. Young, G.A. Price, G.-L. Ingold, G.E. Allen, G.R. Lee, H. Audren, I. Probst, J.P. Dietrich, J. Silterra, J.T. Webber, J. Slavič, J. Nothman, J. Buchner, J. Kulick, J.L. Schönberger, J.V. de Miranda Cardoso, J. Reimer, J. Harrington, J.L.C. Rodríguez, J. Nunez-Iglesias, J. Kuczynski, K. Tritz, M. Thoma, M. Newville, M. Kümmerer, M. Bolingbroke, M. Tartre, M. Pak, N.J. Smith, N. Nowaczyk, N. Shebanov, O. Pavlyk, P.A. Brodtkorb, P. Lee, R.T. McGibbon, R. Feldbauer, S. Lewis, S. Tygier, S. Sievert, S. Vigna, S. Peterson, S. More, T. Pudlik, T. Oshima, T.J. Pingel, T.P. Robitaille, T. Spura, T.R. Jones, T. Cera, T. Leslie, T. Zito, T. Krauss, U. Upadhyay, Y.O. Halchenko, Y. Vázquez-Baeza, Scipy 1.0: fundamental algorithms for scientific computing in python, Nat Methods 17 (2020) 261–272, http://dx.doi.org/10.1038/s41592-019-0686-2.

[51] J.D. Hunter, Matplotlib: A 2D graphics environment, Comput. Sci. Eng. 9 (2007) 90–95, http://dx.doi.org/10.1109/MCSE.2007.55.

[52] D. Oquab, N. Xu, D. Monceau, D.J. Young, Subsurface microstructural changes in a cast heat resisting alloy caused by high temperature corrosion, Corros. Sci. 52 (2010) 255–262, http://dx.doi.org/10.1016/j.corsci.2009.09.014.

[53] A.D. Hwang, Determine circle of intersection of plane and sphere, 2024, https://math.stackexchange.com/q/1218805 (Accessed 23 June 2024).

[54] N. Saunders, A.P. Miodownik, CALPHAD (Calculation of Phase Diagrams): A Comprehensive Guide, Pergamon Press, 1998.

[55] H. Lukas, S.G. Fries, B. Sundman, Computational Thermodynamics - the Calphad Method, Cambridge University Press, 2007.

[56] C.E. Campbell, A new technique for evaluating diffusion mobility parameters, J Phase Equil Diff 26 (2005) 435–440, http://dx.doi.org/10.1007/s11669-005-0031-6.